ACS OMEGA

http://pubs.acs.org/journal/acsodf

Article

Backscattering-Based Discrimination of Microparticles Using an Optofluidic Multiangle Scattering Chip

Reza Ebrahimifard, Peer Erfle, Andreas Dietzel, and Georg Garnweitner*

Cite This: *ACS Omega* 2022, 7, 17519−17527

Read Online

ACCESS | Metrics & More | Article Recommendations | Supporting Information

ABSTRACT: In this research, we designed and fabricated an optofluidic chip for the detection and differentiation of single particles via the combination of backscattered (BSC) and forward-scattered (FSC) or side-scattered (SSC) light intensity. The high sensitivity of BSC light to the refractive index of the particles enabled an effective approach for the differentiation of individual particles based on the type of material. By recording BSC as well as FSC and SSC light intensities from single particles, transiting through the illumination zone in a microfluidic channel, the size and type of material could be detected simultaneously. The analysis of model samples of polystyrene (PS), as a primary microplastic particle, and silica microspheres showed substantially higher BSC signal values of PS because of a larger refractive index compared to the silica. The scatter plots correlating contributions of BSC (FSC−BSC and SSC−BSC) allowed a clear differentiation of PS and silica particles. To demonstrate the great potential of this methodology, two "real-life" samples containing different types of particles were tested as application examples. Commercial toothpaste and peeling gel products, as primary sources of microplastics into effluents, were analyzed via the optofluidic chip and compared to results from scanning electron microscopy. The scattering analysis of the complex samples enabled the detection and simultaneous differentiation of particles such as microplastics according to their differences in the refractive index via distinctive areas of high and low BSC signal values. Hence, the contribution of BSC light measurements in multiangle scattering of single particles realized in an optofluidic chip opens the way for the discrimination of single particles in a liquid medium in manifold fields of application ranging from environmental monitoring to cosmetics.

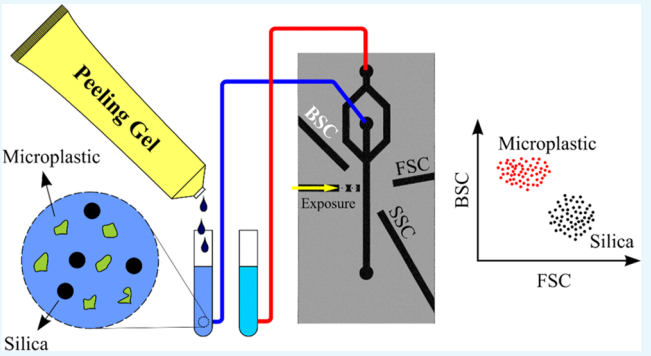

INTRODUCTION

Scattering of light is a powerful characterization method with broad fields of application such as astronomy,[1,2] biology,[3,4] environmental study,[5,6] and particle analysis.[7−11] The latter is based on the sensitivity of the scattering phenomena to the size, morphology, and refractive index of the particles.[12,13] Several examples of the detailed optical scattering analysis of particles are available in the literature, such as size measurement of particles,[5,6,14] investigation of Brownian motion in colloids,[15] investigation of the dynamics of single objects and detection of the particles and aggregates in biological systems,[16,17] and the analysis of nanoparticles.[18,19]

The optical scattering analysis of particles can be performed via ensemble measurement or single-particle counting. The ensemble methods, such as dynamic light scattering (DLS), allow optical scattering analysis of a large number of particles.[20,21] Although the method offers a fast and reliable solution for the particle size distribution analysis, the results are based on ensemble value approximations and general assumptions such as a monomodal particle size distribution, which is not always the case.

In contrast, single-particle detection methods allow discrimination of individual particles with high precision.[22−24] Such an approach has been demonstrated based on microfluidic systems, which quantify nanoparticle fluorescence.[25,26] In addition, microfluidic scatter measurement approach enables the investigation of the chemical and morphological heterogeneity of the individual particles in a dispersion sample. Methods like scattering tracking analysis (STA) can give accurate particle size and distribution based on single-particle movement tracking.[27,28] However, the direct discrimination of particles with different compositions, without using fluorescence dye labeling, would be challenging and the method requires a platform for visualization and image processing for the precise tracking of the moving particles.

In addition to single-particle measurement, the identification and separation of particles based on their material composition is of high importance. The dependency of the scattered light

Received: November 10, 2021
Accepted: April 27, 2022
Published: May 19, 2022

on the refractive index of the particle can be implemented for the discrimination of particles based on their composition. The scattered light can be classified into three different types based on the direction relative to the incident beam: low-angle or forward scattering (FSC), vertical or sideward scattering (SSC), and backward scattering (backscattering, BSC).[29−31] In FSC, diffraction is the major phenomenon, which takes place at the surface and does not interact with the internal structure. Therefore, the FSC signal is highly sensitive to the size of the particles rather than material composition. In SSC, scattering and refraction play a role and therefore, SSC is also influenced by the internal structure of the particle. In BSC, all three scatter mechanisms, namely, diffraction, refraction, and reflection, contribute. Due to multiple internal interactions with the particle material, the internal structure (refractive index) of particles strongly influences the BSC signal and substantial interference phenomena can take place, depending on the size, refractive index, and exposure wavelength.[32,33] Therefore, the BSC measurement strongly depends on the refractive index of the particle.

Static light scattering (SLS) can be implemented for both detection and discrimination of single particles.[26,34,35] For example, flow cytometry allows high-throughput cell counting and sorting based on the SLS principle.[36−40] Conventional flow cytometers use the combination of FSC−SSC as well as fluorescence scatter plots for the optical analysis of the biological cells. Despite several advantages, flow cytometers normally only detect SSC and FSC intensities, and the instruments are bulky and expensive and also challenging to be used for remote or in-line analysis purposes. Accordingly, the capability of BSC signal measurement as well as miniaturization of a cytometry system would afford great advantages for particle discrimination.

The optofluidic chip technology[41−46] provides a miniaturized platform for both optical measurement and fluid manipulation. It allows integrating micron-size optical elements such as microlenses[47] and enables the coupling of the chip to the light source and detectors via optical fibers (OF), thereby external optical elements can be eliminated from the setup, resolving the spatial constraints limiting the proximity of the illumination and BSC detection parts. The other important aspect of the optofluidic technology is the use of the flow focusing technique to create a narrow stream of the sample, which confines the transit of single particles to the focal spot of the incident beam for the scattering analysis and minimizes the concurrent detection of multiple particles.[48,49] The multifunctionality of the optofluidic chip as well as its small size, simple operation, and reliable results allows implementing such systems for various fields of application.

Several works have been presented on miniaturized cytometry systems for the detection and discrimination of blood cells or model particles. In most cases, FSC and SSC signals were recorded,[50−54] and some methods integrated fluorescence analysis for the differentiation of stained cells.[52,55,56]

In this research, a BSC-based optofluidic chip has been designed and realized for the differentiation of single particles in a liquid sample medium. We have implemented BSC besides detection of standard FSC and SSC light intensities (FSC−BSC, SSC−BSC besides standard FSC−SSC scatter plots) to discriminate particles of different materials based on their BSC signal values. Our goal was not only to demonstrate the new technique using model particle samples of PS and silica but also to test its applicability to real-life particle samples of toothpaste and peeling gel to discriminate particles such as microplastics in these products. Due to its flexibility and small size, as well as the standard optical components used, the presented optofluidic chip shows high potential for environmental monitoring applications, in particular the measurement of the concentration of microplastics also in samples where natural inorganic particles such as silica, e.g., from river sands, are present.

MATERIALS AND METHODS

Optofluidic Chip Design and Fabrication. An optofluidic chip has been designed and fabricated to be tailored for the measurement (Figures 1 and S1). Figure 1a shows a sketch

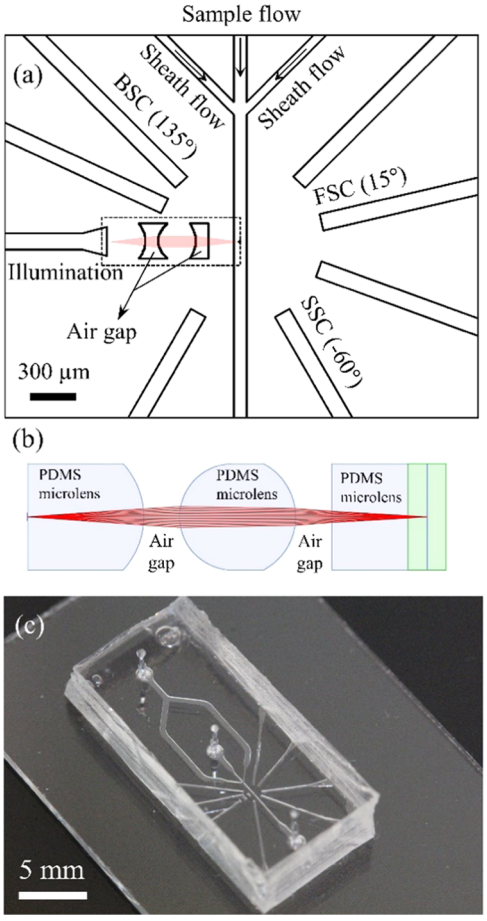

Figure 1. (a) Schematic representation of the optofluidic chip, (b) microlens setup to achieve focusing of the primary beam to the center of the microfluidic channel, and (c) photograph of the optofluidic device.

of the optofluidic chip. The chip comprises two main functional areas of hydrodynamic flow focusing and optical measurement. The hydrodynamic flow focusing part is composed of sample flow and sheath flow channels, into which the sample of dilute particle dispersion and ultra-pure deionized water (DIW) are injected, respectively. All three flows enter a straight channel that passes through the optical measurement zone. The sample flow is narrowed to a certain width by adjusting the flow rates of sample and sheath flows.

The optical measurement zone is composed of an illumination part and a detection part. In the illumination

https://doi.org/10.1021/acsomega.1c06343
ACS Omega 2022, 7, 17519−17527

part, two cylindrical microlenses, using the so-called air gap technique (Figure 1b),[47] were implemented for collimating and focusing the incident light to the middle of the fluid channel, where particles transit. The scattered light of BSC, FSC, and SSC from single particles is collected in different trigonometrical angles of 135, 15, and −60°. Optical fibers (OF) are connected to the optofluidic chip to couple the laser light source and photodetectors for illumination and detection purposes. To this end, the fiber channels integrated into the optofluidic chip were designed to be able to simply and reversibly plug in OF. The ends of the fiber channels for scattering detection are placed at equal distances from the center of the optical focus point in the middle of the flow channel.

The fabrication of the optofluidic chip was carried out via the standard soft lithography technique.[57−59] Details of the design, fabrication process, system assembly, and measurement procedure are explained in the Supporting Information (SI).

Materials. Two different groups of model and real-life samples were measured via the optofluidic chip. For the model samples, aqueous dispersions of PS and silica microspheres with nominal diameters of 10, 5, and 2 μm (all purchased from microparticles GmbH) have been used. Three different groups of samples including monosized, mixed size (Mix-1), and mixed size and material (Mix-2) samples were tested. For the real-life samples, two different health care products of the commercial brands of a toothpaste and peeling gel were investigated. Details of the sample preparation procedure for the optical scattering measurement are given in the SI.

Scanning Electron Microscopy (SEM). SEM and energy-dispersive X-ray spectroscopy (EDS) were performed to determine the morphology and chemical composition of the particles. Details of the sample preparation procedure for SEM/EDS analysis are given in the Supporting Information.

RESULTS AND DISCUSSION

Calculation of Scattering. To investigate the scattering phenomena, the dependence of the scattering efficiency on the particle diameter was calculated through Mie functions for particles with different refractive indices n = 1.45, 1.54, 1.58, and 1.64 (at a wavelength of 780 nm as used in all experiments). By definition, scattering efficiency is the ratio between scattering cross section and geometric cross section.[60−62] The calculations were carried out based on the MATLAB code by Mätzler.[61] Figure 2a shows large fluctuations of the BSC efficiency with close maxima and minima. In certain ranges of particle diameters (2−6 and 2−12 μm), the BSC efficiency of particles with larger refractive indices (1.54, 1.58, and 1.64) is several orders of magnitude higher than for low-refractive-index (1.45) particles. This difference between the BSC efficiencies of particles with high and low refractive indices is significantly larger compared to the difference of scattering efficiencies for particle diameters higher than 1 μm (Figure S2a). This feature of BSC is attributed to the higher sensitivity of BSC light intensity to the internal structure of the particles.

The effect of the scattering angle was investigated by calculating the scattering amplitude at different angles. Figure 2b shows the calculated plot for particles with refractive indices of 1.45 and 1.58 (at 780 nm) and 5 μm diameter corresponding to the model particles of silica and PS (see Figures S2b,c and S3 for 2, 5, and 10 μm diameters). The fluctuation of the scattering amplitude is stronger at higher

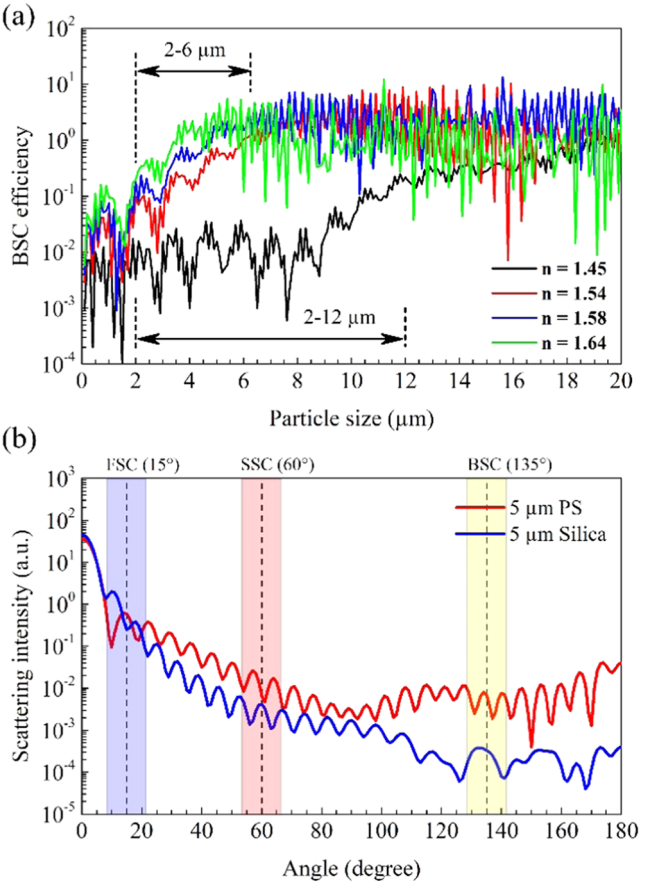

Figure 2. (a) Calculated Mie scattering efficiencies for backscattering light versus particle diameter for materials with different refractive indices of n = 1.45, 1.54, 1.58, and 1.64. (b) Calculated scattering amplitude in different angles for PS (n = 1.58) and silica (n = 1.45) particles with a 5 μm diameter.

angles representing the BSC range. Considering the fabrication constraints, the angles of scattering detection were chosen so that the scattering signal of particles with different refractive indices was the most different. The procedure is explained in detail in the SI.

Model Samples. To investigate the performance of the method, the two model particle systems of silica and PS (as a primary type of microplastic particles)[63] were tested in different particle diameters. Figure 3 shows the voltage-equivalent scattering signal of BSC, FSC, and SSC vs recording time and the combined scatter plots of SSC−BSC, FSC−BSC, and SSC−FSC for PS and silica samples of 10 μm nominal size. For comparison, the analogous plots for particles of 5 and 2 μm nominal size are shown in the Supporting Information (Figures S4 and S5). The recorded scattering signals (Figure 3a,b) consist of a large number of individual peaks that are associated with the scattering from single particles. The level of scattering for fixed experimental parameters (wavelength and power of laser light, flow rate of both sample and side flows, and level of signal amplification factor in detectors) depends on the size and refractive index of the particle.[12,13] Thereby, the smaller particles show substantially lower scattering signal values that nevertheless are clearly distinct from the background noise. A few scattering peaks with a significantly higher intensity compared to the normal scattering signals may be attributed to the presence of agglomerated particles, different

https://doi.org/10.1021/acsomega.1c06343
ACS Omega 2022, 7, 17519−17527

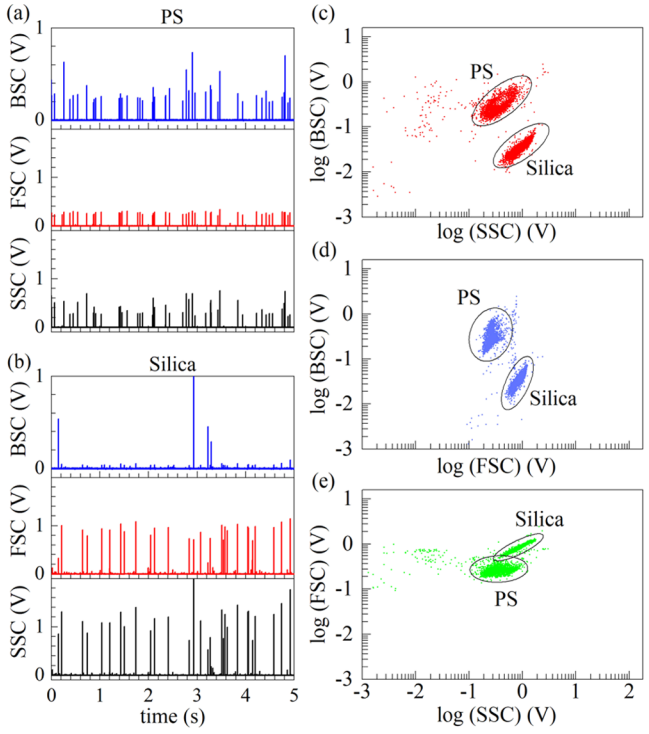

Figure 3. Voltage-equivalent scattering signal of BSC, FSC, and SSC versus recording time for (a) PS and (b) silica microspheres of 10 μm nominal diameter. The corresponding (c) SSC−BSC, (d) FSC−BSC, and (e) SSC−FSC scatter plots of the measured particle in logarithmic scale.

positions of particles across the channel depth, and the quantity of the collected signal by the OF, which can be influenced by the intensity pattern of the scatter signal around the particle at different angles.

Considering each particle size category of 10, 5, and 2 μm (Figures 3, S4, and S5), the BSC signal value of the PS is higher than that for silica particles. These results are in accordance with scattering efficiency calculations (Figure 2). As the refractive index of PS (n = 1.58) is higher than the one of silica (n = 1.45), the BSC efficiency and, consequently, the BSC light intensity are higher for the PS than for silica. To investigate the accordance between measured values and the calculations according to the Mie theory, the BSC, SSC, and FSC scattering intensity was plotted versus particle diameter for both PS and silica particles (Figure S3). While the absolute values cannot be correlated as the measured values are given in V and are detector-dependent, the results show that the measured values follow the general trend of the Mie calculation for BSC, SSC, and FSC. It is important to note that the calculated value is the integral of the calculated scattering intensity (Figure S2) around measurement angles of 15, 60, and 135° with an interval of about ±6° because the optical fibers collect the scattering signal in this angular range (numerical aperture of 0.1). Some deviations, in particular in the SSC and BSC signal trends of the silica particles, are attributed to the experimental conditions and the signal detection. Several factors such as lower signal-to-noise ratio (SNR) of the smaller particles, tolerance of particle size, transit of particles in different channel heights in the exposure zone, and tolerance of the optical elements are not taken into account for the calculation. In addition, a different type of photodetector was used for the detection of the FSC signal compared to the SSC and BSC, leading to signals of about 100× lower voltage than expected.

The difference in the amplitude of the measured scatter signal between PS and silica particles becomes particularly visible in two-parameter scatter plots. Figure 3c−e shows the scatter plots and location of the 10 μm-sized PS and silica samples based on the distribution of scattering signal values (clouds). Each point in the scatter plots corresponds to the scattering signal intensities from a single particle. In comparison to the FSC and SSC signal intensities, the BSC signal amplitude of PS particles is substantially higher than that for silica. Hence, PS and silica samples are more easily distinguishable in plots with the contribution of BSC (FSC−BSC and SSC−BSC) compared to the SSC−FSC. Similar results are obtained for smaller particle diameters of 5 and 2 μm for both PS and silica (Figures S4 and S5). Under a similar measurement condition, while the BSC signal of the PS sample is always higher than that for silica, the FSC and SSC behave differently. In the samples with a 10 μm particle diameter, both the FSC and SSC signal amplitudes of silica are higher than PS. In the samples with a 5 μm particle diameter, the FSC signal of PS and silica are relatively similar, while the SSC signal amplitude of PS is significantly higher than that for silica. In the samples of 2 μm particle diameter, both the FSC and SSC signal amplitudes of PS are significantly higher than for silica. Therefore, for the investigated particle diameters of 2, 5, and 10 μm, BSC demonstrates a better foundation for the discrimination of particles with a large difference in the refractive index, such as PS (n = 1.58) and silica (n = 1.45).

As a statistical analysis, the coefficient of variation (CV), which is defined as the standard deviation divided by the mean of the measured scatter signal amplitude, was calculated by approximating a Gaussian distribution of the scatter data (Table S1). In general, the calculated CVs for FSC are lower than those for the SSC and BSC scatter data. Considering the tolerance of particle diameter, this can be attributed to the larger fluctuation of scattering efficiency of BSC and SSC compared to the FSC signal (Figure 2). The samples with a larger particle diameter show lower CV values compared to the smaller ones, which can be attributed to the higher SNR (Table S2). In addition, the CV values for BSC (5 and 2 μm) and SSC (2 μm) of the silica particles are significantly larger than the other data because of the low SNR. The calculated CV values of the scattering measurements are comparable to the results obtained with other on-chip cytometers,[64−66] and the scatter plots (Figures 3c−e, S4c, and S5c) show a reliable separation of the cloud regions for each particle size. However, several strategies such as using three-dimensional (3D) hydrodynamic focusing, as recently demonstrated in a nanoparticle precipitation device,[67] and beam modifications will need to be implemented to further improve the CV values.[50,68]

In contrast to these model samples, samples from industrial products or from environmental monitoring may contain particles of different sizes. Therefore, the mixed model samples were designed to simulate the conditions of real samples. Figure 4a,b shows the FSC−BSC scatter plots of mixed PS and mixed silica samples (Mix-1) containing particles with different diameters. The scatter plots of SSC−BSC and SSC−FSC are demonstrated in the Supporting Information (Figure S6a,b). As discussed above, the scatter plots of the measurements of single-size particle samples showed that the scattering signal distribution for each particle size occupies a particular region in

https://doi.org/10.1021/acsomega.1c06343
ACS Omega 2022, 7, 17519−17527

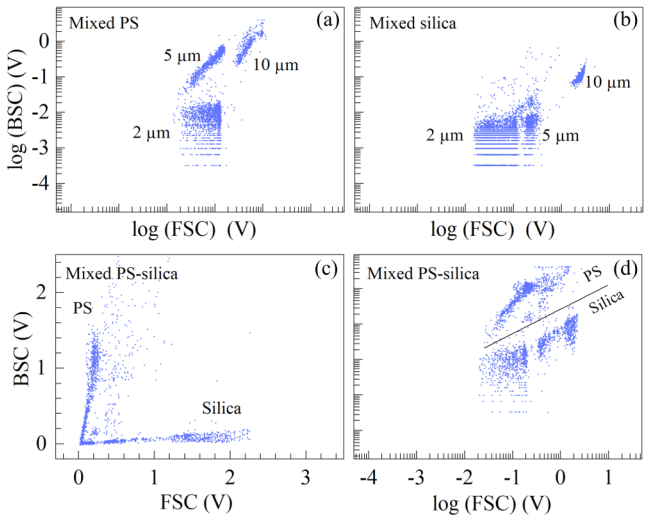

Figure 4. FSC−BSC scatter plots of (a) mixed PS and (b) mixed silica particle samples (Mix-1) in logarithmic scale. Scatter plots of mixed PS-silica samples (Mix-2) in (c) linear and (d) logarithmic scales.

the scatter plot. The scatter plots of the mixed samples of PS and silica each show three separate clouds that are correlated with the signals of particles with the three different diameters of 10, 5, and 2 μm. Accordingly, the results clearly prove the discrimination of particles with different sizes in both the PS and silica samples. In general, as the particle size decreases, the scattering intensity decreases and the scatter distribution moves from the top-right to the bottom-left of the scatter plots.

Many natural samples contain particles of different materials. Therefore, a mixture of PS and silica particles (Mix-2) with different sizes of 10, 5, and 2 μm was prepared to mimic such samples. Figures 4c,d and S6c,d show the scatter plot of Mix-2 in both logarithm and linear-scale representation. The FSC−BSC and SSC−BSC (Figure S6c,d) scatter plots allow a clear differentiation between the PS and silica samples, while in the SSC−FSC plot (Figure S6c,d), the difference is not distinguishable. This becomes clearer in the linear-scale scatter plot (Figure 4c) that shows a vertical and a horizontal arm-shaped scattering value distribution that are clearly distinct and can be assigned to the PS and silica samples, respectively. The scatter signal regions of the PS and silica particles in the FSC−BSC scatter plot is separated more clearly compared to the SSC−BSC and SSC−FSC plots (Figure S6c,d) because FSC is more sensitive to the particle size, while BSC is determined by both size and particularly the internal structure (refractive index) of the particle. The SSC signal has similar characteristics to BSC but is less sensitive to the internal structure. Accordingly, BSC and FSC share fewer common features and the FSC−BSC plots can better represent the material differences.

Toothpaste. As a more realistic particle sample with a high refractive index, dicalcium phosphate particles (n = 1.58−1.64)[69] in a commercial brand toothpaste were tested. Figure S7 shows the result of SEM and EDS analyses, proving that dicalcium phosphate particles of different morphologies and sizes were present in the sample. Figure S8 presents the scatter plots (linear scale) and their relative kernel density plots (in logarithmic scale) of the optofluidic measurement. The FSC−BSC plot shows a vertical arm-shaped scattering signal distribution with partially relatively high BSC signal values that can be attributed to the dicalcium phosphate particles. Hence, also for nonspherical particles, the hypothesis of high sensitivity of BSC to the refractive index is demonstrated (see the SI for further details).

Peeling Gel. To demonstrate the distinction of inorganic and organic (microplastic) particle constituents of a sample, the analysis of a commercial peeling gel sample by the optofluidic chip setup was performed. Peeling gels are facial exfoliating products, containing particles and scrubbing ingredients that make the skin smoother by removing dead cells.[70] The particulate ingredients are composed of natural and synthetic compounds in the size range of hundreds to tens of microns.[71] One of the most critical ingredients of facial exfoliators are such micron-size plastic particles (microplastics), which are considered a potential health threat to living organisms and humans. The microplastics can enter the food chain through different sources and procedures. It has been shown that facial exfoliators are primary sources of microplastics released into effluents through washing the face after usage, which can end up in the marine environment.[72] Microplastics with a size of less than 100 μm can be taken up by planktonic organisms and transferred to the human body through the food chain.[70,73,74] In addition, the uptake of the microplastics by living cells leads to toxic effects on cell functionality.[75−77]

A commercial brand peeling gel product was purchased and diluted for the measurement. To investigate the morphology, size, and composition of the peeling gel particles, SEM and EDS analyses were performed (Figures 5a−e and S9). Different types of particles with different sizes and morphologies are proven by the analysis, including silica-based particles and micron-sized organic particles, which are assumed to be microplastics. The microplastic particles have different morphologies including spherical and rodlike shapes, with a particle size in the range of 5−500 μm.

The optical scattering measurement is carried out on an aqueous dispersion of the peeling gel sample. Figures 5f,g and S10 show the scatter and Kernel density plots of measured particles. Both the FSC−BSC and the SSC−BSC scatter plots (Figure S10) show two arm-shaped scattering signal distributions, which analogously to the previously investigated model samples can be attributed to the presence of particles with high and low refractive indices, based on the calculation of the BSC efficiency (Figure 2).

The microplastic particles as abrasive scrubs in peeling gels are majorly composed of polyethylene, which has a refractive index of n = 1.54.[70,72] Based on the morphological features from the SEM images, the peeling gel could contain both synthetic (microspheres) and natural (random morphology with porous structure) silica microparticles. Similar to the model samples, the synthetic silica has a refractive index of n = 1.45. The refractive index of natural silica is basically n = 1.54; however, the porous structure of the silica particles in the peeling gel could yield a lower refractive index based on the effective optical properties approximation of porous materials.[78−80] Thus, the substitution of a portion of silica (porosity content) with a material of lower refractive index yields an overall lower refractive index. For example, porous silica with 20% porosity that is filled by water (large pores) or air (small pores) under specific conditions results in a calculated refractive index of n = 1.50 and 1.45, respectively. Thereby, higher porosity results in a lower refractive index. It is however important to note that small differences in the refractive index

https://doi.org/10.1021/acsomega.1c06343
ACS Omega 2022, 7, 17519−17527

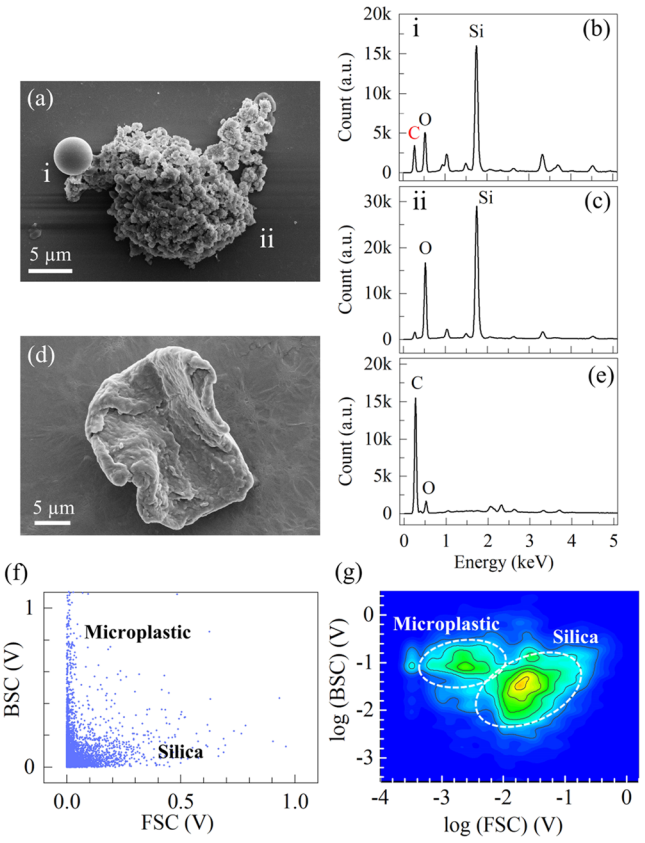

Figure 5. SEM and EDS results of (a–c) silica-based particles and (d–e) microplastic particles in peeling gel samples. FSC–BSC (f) scatter plot and (g) Kernel density plot in logarithmic scale (the red-marked peak of C in the EDS plot (b) is attributed to the carbon tape sample holder; a glass sample holder was used for (e)).

can result in a large difference in the BSC signal, as is demonstrated in Figure 2b, and a nonuniform refractive index distribution within the particle as well as other factors such as particle and pore sizes and the choice of mixing rule can thus lead to large deviations.[81] However, considering the size of the natural silica particles (>5 μm) and the range of the calculated refractive index of porous silica particles, the FSC–BSC plot of Figure 5f can be explained. Accordingly, the regions of high and low BSC signal values in the FSC–BSC and SSC–BSC scatter plots could be justified by the presence of high-refractive-index microplastic and lower-refractive-index synthetic and natural porous silica particles. The SSC–FSC plot does not show a comparable separation of the data into regions that would allow discrimination of the particle type. Therefore, similarly to our previous discussion, the scatter plot combining FSC and BSC is identified as the best scattering signal representation for the evaluation of particle type.

CONCLUSIONS

An optofluidic chip was designed and realized for the detection and differentiation of single particles, implementing a back-scattering-based measurement technique. Calculated Mie scattering efficiencies showed a substantial difference between the BSC efficiency values of particles with high and low refractive indices. The backscattering detection angle was implemented according to the calculated correlation of scattering amplitude against angle, while fabrication constraints needed to be taken into account. The combination of our BSC technique, as a material-sensitive parameter, with standard FSC and SSC introduced a new multiparametric single-particle discrimination tool for particle discrimination based on differences in refractive index.

The measurement of model samples of PS and silica microspheres with nominal diameters of 10, 5, and 2 μm allowed a clear differentiation of PS and silica particles in the FSC–BSC and SSC–BSC plots because of the higher refractive index of the PS particles, while the standard SSC–FSC plot hardly allows a distinction of the measured particles into different material types.

Subsequently, we presented the analysis of samples of a commercial toothpaste and peeling gel. The morphology and composition of the particles in these "real-life" samples were analyzed via SEM and EDS measurements. The toothpaste sample (containing high-refractive-index dicalcium phosphate particles) showed high BSC signal values in the FSC–BSC scatter plot. Analysis of the peeling gel product revealed a distinguished two arm-scattering signal distribution in the FSC–BSC scatter plot, which could be separately attributed to the microplastic and silica particles present in the sample, respectively.

The optofluidic chip-based method presented here holds promise for an accurate evaluation of diverse particle samples with different refractive indices in liquid dispersion and could be further improved in the future by implementing polarized light in exposure and detection, illumination of multi-wavelength light, and using 3D flow focusing. In comparison to classical flow cytometers that only measure FSC and SSC, our BSC-based multiangle scattering measurement chip allows differentiation of particles at significantly higher resolution. The method can thus open the way for single-particle detection in environmental studies and water resource research, the cosmetics and pharmaceutical industries, and enables a flexible and mobile analysis to investigate synthetic and natural particles.

ASSOCIATED CONTENT

Supporting Information

The Supporting Information is available free of charge at https://pubs.acs.org/doi/10.1021/acsomega.1c06343.

Experimental details, scattering signals of particles with 5 and 2 μm diameters, SSC–FSC and SSC–BSC scatter plots, calculated coefficient of variation percentage (CV %), calculated signal-to-noise ratio (SNR), and details of toothpaste sample (PDF)

AUTHOR INFORMATION

Corresponding Author

Georg Garnweitner − *Institute for Particle Technology, Technische Universität Braunschweig, 38104 Braunschweig, Germany; Laboratory for Emerging Nanometrology, Technische Universität Braunschweig, 38106 Braunschweig, Germany;* orcid.org/0000-0002-7499-4947; Phone: +49 531 3919615; Email: g.garnweitner@tu-braunschweig.de

Authors

Reza Ebrahimifard − *Institute for Particle Technology, Technische Universität Braunschweig, 38104 Braunschweig, Germany; Laboratory for Emerging Nanometrology, Technische Universität Braunschweig, 38106 Braunschweig, Germany*

https://doi.org/10.1021/acsomega.1c06343
ACS Omega 2022, 7, 17519−17527

Peer Erfle − *Institute of Microtechnology, Technische Universität Braunschweig, 38092 Braunschweig, Germany;* orcid.org/0000-0003-4503-6392

Andreas Dietzel − *Institute of Microtechnology, Technische Universität Braunschweig, 38092 Braunschweig, Germany; Laboratory for Emerging Nanometrology, Technische Universität Braunschweig, 38106 Braunschweig, Germany*

Complete contact information is available at: https://pubs.acs.org/10.1021/acsomega.1c06343

Author Contributions

R.E. designed the experiments, performed the experiments, and wrote the paper. P.E. supported the fabrication of the optofluidic chip and the setup of the experimental system. A.D. and G.G. conceived and supervised the research project and corrected the manuscript. All authors have given approval to the final version of the manuscript.

Notes

The authors declare no competing financial interest.

■ ACKNOWLEDGMENTS

This research was funded by Niedersächsisches Ministerium für Wissenschaft und Kultur through the "Quantum- and Nano-Metrology (QUANOMET)" initiative (ZN3245) within the project NP-1. We furthermore acknowledge support of this publication by the Open Access Publication Funds of Technische Universität Braunschweig.

■ ABBREVIATIONS

BSC, backscattering; FSC, forward scattering; SSC, side scattering; SLS, static light scattering; DLS, dynamic light scattering; OF, optical fiber; PS, polystyrene bead; PDMS, polydimethylsiloxane; SEM, scanning electron microscopy; EDS, energy-dispersive X-ray spectroscopy; CV, coefficient of variation; SNR, signal-to-noise ratio; DIW, deionized water

■ REFERENCES

(1) Heese, S.; Wolf, S.; Brauer, R. Characterization of Mid-Infrared Polarization Due to Scattering in Protoplanetary Disks. *Astron. Astrophys.* **2020**, *634*, No. A129.

(2) Porco, C. C.; Weiss, J. W.; Richardson, D. C.; Dones, L.; Quinn, T.; Throop, H. Simulations of the Dynamical and Light-Scattering Behavior of Saturn's Rings and the Derivation of Ring Particle and Disk Properties. *Astron. J.* **2008**, *136*, 2172−2200.

(3) Jacques, S. L. Corrigendum: Optical Properties of Biological Tissues: A Review. *Phys. Med. Biol.* **2013**, *58*, 5007−5008.

(4) Dannhauser, D.; Rossi, D.; Causa, F.; Memmolo, P.; Finizio, A.; Wriedt, T.; Hellmers, J.; Eremin, Y.; Ferraro, P.; Netti, P. A. Optical Signature of Erythrocytes by Light Scattering in Microfluidic Flows. *Lab Chip* **2015**, *15*, 3278−3285.

(5) Sullivan, J. M.; Twardowski, M. S.; Donaghay, P. L.; Freeman, S. A. Use of Optical Scattering to Discriminate Particle Types in Coastal Waters. *Appl. Opt.* **2005**, *44*, 1667.

(6) Koestner, D.; Stramski, D.; Reynolds, R. A. Assessing the Effects of Particle Size and Composition on Light Scattering through Measurements of Size-fractionated Seawater Samples. *Limnol. Oceanogr.* **2020**, *65*, 173−190.

(7) Carvalho, P. M.; Felício, M. R.; Santos, N. C.; Gonçalves, S.; Domingues, M. M. Application of Light Scattering Techniques to Nanoparticle Characterization and Development. *Front. Chem.* **2018**, *6*, No. 237.

(8) Jones, A. R. Light Scattering for Particle Characterization. *Prog. Energy Combust. Sci.* **1999**, *25*, 1−53.

(9) Xu, R. Light Scattering: A Review of Particle Characterization Applications. *Particuology* **2015**, *18*, 11−21.

(10) Kovářík, T.; Bělský, P.; Rieger, D.; Ilavsky, J.; Jandová, V.; Maas, M.; Šutta, P.; Pola, M.; Medlín, R. Particle Size Analysis and Characterization of Nanodiamond Dispersions in Water and Dimethylformamide by Various Scattering and Diffraction Methods. *J. Nanopart. Res.* **2020**, *22*, No. 34.

(11) Shi, X.; Gao, R.; Ying, Y.-L.; Si, W.; Chen, Y.-F.; Long, Y.-T. A Scattering Nanopore for Single Nanoentity Sensing. *ACS Sensors* **2016**, *1*, 1086−1090.

(12) Yguerabide, J.; Yguerabide, E. E. Light-Scattering Submicroscopic Particles as Highly Fluorescent Analogs and Their Use as Tracer Labels in Clinical and Biological Applications. *Anal. Biochem.* **1998**, *262*, 157−176.

(13) Yguerabide, J.; Yguerabide, E. E. Light-Scattering Submicroscopic Particles as Highly Fluorescent Analogs and Their Use as Tracer Labels in Clinical and Biological Applications. *Anal. Biochem.* **1998**, *262*, 137−156.

(14) Lim, J.; Yeap, S. P.; Che, H. X.; Low, S. C. Characterization of Magnetic Nanoparticle by Dynamic Light Scattering. *Nanoscale Res. Lett.* **2013**, *8*, No. 381.

(15) Hassan, P. A.; Rana, S.; Verma, G. Making Sense of Brownian Motion: Colloid Characterization by Dynamic Light Scattering. *Langmuir* **2015**, *31*, 3−12.

(16) Hoover, B. M.; Murphy, R. M. Evaluation of Nanoparticle Tracking Analysis for the Detection of Rod-Shaped Particles and Protein Aggregates. *J. Pharm. Sci.* **2020**, *109*, 452−463.

(17) Ye, Z.; Wang, X.; Xiao, L. Single-Particle Tracking with Scattering-Based Optical Microscopy. *Anal. Chem.* **2019**, *91*, 15327−15334.

(18) Guerra, L. F.; Muir, T. W.; Yang, H. Single-Particle Dynamic Light Scattering: Shapes of Individual Nanoparticles. *Nano Lett.* **2019**, *19*, 5530−5536.

(19) Guerra, L. F.; Muir, T. W.; Yang, H. Determining the Spheroid Geometry of Individual Metallic Nanoparticles by Two-Dimensional Single-Particle Dynamic Light Scattering. *J. Phys. Chem. C* **2019**, *123*, 18565−18572.

(20) Balog, S.; Rodriguez-Lorenzo, L.; Monnier, C. A.; Obiols-Rabasa, M.; Rothen-Rutishauser, B.; Schurtenberger, P.; Petri-Fink, A. Characterizing Nanoparticles in Complex Biological Media and Physiological Fluids with Depolarized Dynamic Light Scattering. *Nanoscale* **2015**, *7*, 5991−5997.

(21) Zhang, B.; Wang, C.; Song, Z.-L.; Xu, C.-L.; He, Z.-Z. Determination of Particle Size Distribution Based on Dynamic Light Scattering Measurements in the near Field. *Opt. Lasers Eng.* **2020**, *127*, No. 105980.

(22) Pollard, M.; Hunsicker, E.; Platt, M. A Tunable Three-Dimensional Printed Microfluidic Resistive Pulse Sensor for the Characterization of Algae and Microplastics. *ACS Sensors* **2020**, *5*, 2578−2586.

(23) Colson, B. C.; Michel, A. P. M. Flow-Through Quantification of Microplastics Using Impedance Spectroscopy. *ACS Sensors* **2021**, *6*, 238−244.

(24) Liu, Y.; Xu, C.; Gao, T.; Chen, X.; Wang, J.; Yu, P.; Mao, L. Sizing Single Particles at the Orifice of a Nanopipette. *ACS Sensors* **2020**, *5*, 2351−2358.

(25) Bolze, H.; Erfle, P.; Riewe, J.; Bunjes, H.; Dietzel, A.; Burg, T. A Microfluidic Split-Flow Technology for Product Characterization in Continuous Low-Volume Nanoparticle Synthesis. *Micromachines* **2019**, *10*, 179.

(26) Yan, Y.; Meng, L.; Zhang, W.; Zheng, Y.; Wang, S.; Ren, B.; Yang, Z.; Yan, X. High-Throughput Single-Particle Analysis of Metal-Enhanced Fluorescence in Free Solution Using Ag@SiO 2 Core−Shell Nanoparticles. *ACS Sensors* **2017**, *2*, 1369−1376.

(27) Kerkhoff, Y.; Block, S. Analysis and Refinement of 2D Single-Particle Tracking Experiments. *Biointerphases* **2020**, *15*, No. 021201.

(28) Kubler, R. F.; Rotinat, R.; Badreddine, J.; Puydt, Q. Experimental Analysis of the Shot Peening Particle Stream Using

Particle Tracking and Digital Image Correlation Techniques. *Exp. Mech.* **2020**, *60*, 429−443.
(29) Miroslaw Jonasz, G. F. *Light Scattering by Paricles in Water: Theoretical and Experimental Foundations*; Elsevier Science, 2011.
(30) Usowicz, B. Backscattering. In *Analytical Biochemistry*, Elsevier: Bern, Switzerland, 2011; Vol. *262*, pp 59−60.
(31) Huang, C. Z.; Ling, J.; Wang, J. *Elastic Light Scattering Spectrometry*, De Gruyter, 2018.
(32) Kerker, M. Elastic and Inelastic Light Scattering in Flow Cytometry. *Cytometry* **1983**, *4*, 1−10.
(33) Sloot, P. M. A.; Figdor, C. G. Elastic Light Scattering from Nucleated Blood Cells: Rapid Numerical Analysis. *Appl. Opt.* **1986**, *25*, 3559.
(34) Chen, C.; Zhu, S.; Wang, S.; Zhang, W.; Cheng, Y.; Yan, X. Multiparameter Quantification of Liposomal Nanomedicines at the Single-Particle Level by High-Sensitivity Flow Cytometry. *ACS Appl. Mater. Interfaces* **2017**, *9*, 13913−13919.
(35) Makra, I.; Terejánszky, P.; Gyurcsányi, R. E. A Method Based on Light Scattering to Estimate the Concentration of Virus Particles without the Need for Virus Particle Standards. *MethodsX* **2015**, *2*, 91−99.
(36) Dragovic, R. A.; Southcombe, J. H.; Tannetta, D. S.; Redman, C. W. G.; Sargent, I. L. Multicolor Flow Cytometry and Nanoparticle Tracking Analysis of Extracellular Vesicles in the Plasma of Normal Pregnant and Pre-Eclamptic Women[1]. *Biol. Reprod.* **2013**, *89*, 1−12.
(37) Zucker, R. M.; Ortenzio, J. N. R.; Boyes, W. K. Characterization, Detection, and Counting of Metal Nanoparticles Using Flow. *Cytometry, Part A* **2016**, *89*, 169−183.
(38) Lo Giudice, M. C.; Herda, L. M.; Polo, E.; Dawson, K. A. In Situ Characterization of Nanoparticle Biomolecular Interactions in Complex Biological Media by Flow Cytometry. *Nat. Commun.* **2016**, *7*, No. 13475.
(39) Salvati, A.; Nelissen, I.; Haase, A.; Åberg, C.; Moya, S.; Jacobs, A.; Alnasser, F.; Bewersdorff, T.; Deville, S.; Luch, A.; Dawson, K. A. Quantitative Measurement of Nanoparticle Uptake by Flow Cytometry Illustrated by an Interlaboratory Comparison of the Uptake of Labelled Polystyrene Nanoparticles. *NanoImpact* **2018**, *9*, 42−50.
(40) Zhao, Y.; Lin, C.; Wu, P.; Chen, X.; Zhao, Y.; Li, Y.; Chen, L.; Nilsson, M.; Ke, R. Single Cell RNA Expression Analysis Using Flow Cytometry Based on Specific Probe Ligation and Rolling Circle Amplification. *ACS Sensors* **2020**, *5*, 3031−3036.
(41) Fan, X.; Yun, S.-H. The Potential of Optofluidic Biolasers. *Nat. Methods* **2014**, *11*, 141−147.
(42) Fan, X.; White, I. M. Optofluidic Microsystems for Chemical and Biological Analysis. *Nat. Photonics* **2011**, *5*, 591−597.
(43) Nguyen, N.-T. Micro-Optofluidic Lenses: A Review. *Biomicrofluidics* **2010**, *4*, No. 031501.
(44) Psaltis, D.; Quake, S. R.; Yang, C. Developing Optofluidic Technology through the Fusion of Microfluidics and Optics. *Nature* **2006**, *442*, 381−386.
(45) Levy, U.; Shamai, R. Tunable Optofluidic Devices. *Microfluid. Nanofluid.* **2008**, *4*, 97−105.
(46) Mei, H.; Pan, J.; Zhang, Z.; Zhang, L.; Tong, L. Coiled Optical Nanofiber for Optofluidic Absorbance Detection. *ACS Sensors* **2019**, *4*, 2267−2271.
(47) Yang, H.; Gijs, M. A. M. Micro-Optics for Microfluidic Analytical Applications. *Chem. Soc. Rev.* **2018**, *47*, 1391−1458.
(48) Daniele, M. A.; Boyd, D. A.; Mott, D. R.; Ligler, F. S. 3D Hydrodynamic Focusing Microfluidics for Emerging Sensing Technologies. *Biosens. Bioelectron.* **2015**, *67*, 25−34.
(49) Lu, M.; Ozcelik, A.; Grigsby, C. L.; Zhao, Y.; Guo, F.; Leong, K. W.; Huang, T. J. Microfluidic Hydrodynamic Focusing for Synthesis of Nanomaterials. *Nano Today* **2016**, *11*, 778−792.
(50) Zhao, Y.; Li, Q.; Hu, X. Universally Applicable Three-Dimensional Hydrodynamic Focusing in a Single-Layer Channel for Single Cell Analysis. *Anal. Methods* **2018**, *10*, 3489−3497.
(51) Zhao, Y.; Li, Q.; Hu, X.; Lo, Y. Microfluidic Cytometers with Integrated On-Chip Optical Systems for Red Blood Cell and Platelet Counting. *Biomicrofluidics* **2016**, *10*, No. 064119.
(52) Nawaz, A. A.; Nissly, R. H.; Li, P.; Chen, Y.; Guo, F.; Li, S.; Shariff, Y. M.; Qureshi, A. N.; Wang, L.; Huang, T. J. Immunological Analyses of Whole Blood via "Microfluidic Drifting" Based Flow Cytometric Chip. *Ann. Biomed. Eng.* **2014**, *42*, 2303−2313.
(53) Spencer, D.; Elliott, G.; Morgan, H. A Sheath-Less Combined Optical and Impedance Micro-Cytometer. *Lab Chip* **2014**, *14*, 3064−3073.
(54) Mao, X.; Nawaz, A. A.; Lin, S.-C. S.; Lapsley, M. I.; Zhao, Y.; McCoy, J. P.; El-Deiry, W. S.; Huang, T. J. An Integrated, Multiparametric Flow Cytometry Chip Using "Microfluidic Drifting" Based Three-Dimensional Hydrodynamic Focusing. *Biomicrofluidics* **2012**, *6*, No. 024113.
(55) Barat, D.; Spencer, D.; Benazzi, G.; Mowlem, M. C.; Morgan, H. Simultaneous High Speed Optical and Impedance Analysis of Single Particles with a Microfluidic Cytometer. *Lab Chip* **2012**, *12*, 118−126.
(56) Watts, B. R.; Zhang, Z.; Xu, C.-Q.; Cao, X.; Lin, M. Integration of Optical Components On-Chip for Scattering and Fluorescence Detection in an Optofluidic Device. *Biomed. Opt. Express* **2012**, *3*, 2784.
(57) Kim, P.; Kwon, K. W.; Park, M. C.; Lee, S. H.; Kim, S. M.; Suh, K. Y. Soft Lithography for Microfluidics: A Review. *Biochip J.* **2008**, *2*, 1−11.
(58) Sia, S. K.; Whitesides, G. M. Microfluidic Devices Fabricated in Poly(Dimethylsiloxane) for Biological Studies. *Electrophoresis* **2003**, *24*, 3563−3576.
(59) Kane, R. S.; Stroock, A. D.; Li Jeon, N.; Ingber, D. E.; Whitesides, G. M. Soft Lithography and Microfluidics. In *Optical Biosensors*, Elsevier, 2002; pp 571−595.
(60) Platt, C. M. R.; Collins, R. L. LIDAR | Backscatter. In *Encyclopedia of Atmospheric Sciences*, Elsevier, 2015; Vol. 3, pp 270−276.
(61) Mätzler, C. *MATLAB Functions for Mie Scattering and Absorption*, version 2; Institute of Applied Physics, University of Bern: Switzerland, 2002.
(62) Welsh, J. A.; Horak, P.; Wilkinson, J. S.; Ford, V. J.; Jones, J. C.; Smith, D.; Holloway, J. A.; Englyst, N. A. FCM PASS Software Aids Extracellular Vesicle Light Scatter Standardization. *Cytometry, Part A* **2020**, *97*, 569−581.
(63) Hwang, J.; Choi, D.; Han, S.; Jung, S. Y.; Choi, J.; Hong, J. Potential Toxicity of Polystyrene Microplastic Particles. *Sci. Rep.* **2020**, *10*, No. 7391.
(64) Wang, Z.; El-Ali, J.; Engelund, M.; Gotsæd, T.; Perch-Nielsen, I. R.; Mogensen, K. B.; Snakenborg, D.; Kutter, J. P.; Wolff, A. Measurements of Scattered Light on a Microchip Flow Cytometer with Integrated Polymer Based Optical Elements. *Lab Chip* **2004**, *4*, 372−377.
(65) Rosenauer, M.; Buchegger, W.; Finoulst, I.; Verhaert, P.; Vellekoop, M. Miniaturized Flow Cytometer with 3D Hydrodynamic Particle Focusing and Integrated Optical Elements Applying Silicon Photodiodes. *Microfluid. Nanofluid.* **2011**, *10*, 761−771.
(66) Chen, H.-T.; Wang, Y.-N. Optical Microflow Cytometer for Particle Counting, Sizing and Fluorescence Detection. *Microfluid. Nanofluid.* **2009**, *6*, 529−537.
(67) Lorenz, T.; Bojko, S.; Bunjes, H.; Dietzel, A. An Inert 3D Emulsification Device for Individual Precipitation and Concentration of Amorphous Drug Nanoparticles. *Lab Chip* **2018**, *18*, 627−638.
(68) Watts, B. R.; Zhang, Z.; Xu, C.-Q.; Cao, X.; Lin, M. A Method for Detecting Forward Scattering Signals On-Chip with a Photonic-Microfluidic Integrated Device. *Biomed. Opt. Express* **2013**, *4*, 1051.
(69) Pierre, P. D. S. S. The Preparation of Dicalcium Phosphate Dihydrate and Calcium Pyrophosphate. *J. Am. Chem. Soc.* **1955**, *77*, 2197−2198.
(70) Chang, M. Reducing Microplastics from Facial Exfoliating Cleansers in Wastewater through Treatment versus Consumer Product Decisions. *Mar. Pollut. Bull.* **2015**, *101*, 330−333.

https://doi.org/10.1021/acsomega.1c06343
ACS Omega 2022, 7, 17519−17527

(71) Kozlowska, J.; Prus, W.; Stachowiak, N. Microparticles Based on Natural and Synthetic Polymers for Cosmetic Applications. *Int. J. Biol. Macromol.* **2019**, *129*, 952−956.
(72) Lei, K.; Qiao, F.; Liu, Q.; Wei, Z.; Qi, H.; Cui, S.; Yue, X.; Deng, Y.; An, L. Microplastics Releasing from Personal Care and Cosmetic Products in China. *Mar. Pollut. Bull.* **2017**, *123*, 122−126.
(73) Fendall, L. S.; Sewell, M. A. Contributing to Marine Pollution by Washing Your Face: Microplastics in Facial Cleansers. *Mar. Pollut. Bull.* **2009**, *58*, 1225−1228.
(74) Godoy, V.; Martín-Lara, M. A.; Calero, M.; Blázquez, G. Physical-Chemical Characterization of Microplastics Present in Some Exfoliating Products from Spain. *Mar. Pollut. Bull.* **2019**, *139*, 91−99.
(75) von Moos, N.; Burkhardt-Holm, P.; Köhler, A. Uptake and Effects of Microplastics on Cells and Tissue of the Blue Mussel Mytilus Edulis L. after an Experimental Exposure. *Environ. Sci. Technol.* **2012**, *46*, 11327−11335.
(76) Schirinzi, G. F.; Pérez-Pomeda, I.; Sanchís, J.; Rossini, C.; Farré, M.; Barceló, D. Cytotoxic Effects of Commonly Used Nanomaterials and Microplastics on Cerebral and Epithelial Human Cells. *Environ. Res.* **2017**, *159*, 579−587.
(77) Hwang, J.; Choi, D.; Han, S.; Choi, J.; Hong, J. An Assessment of the Toxicity of Polypropylene Microplastics in Human Derived Cells. *Sci. Total Environ.* **2019**, *684*, 657−669.
(78) Garahan, A.; Pilon, L.; Yin, J.; Saxena, I. Effective Optical Properties of Absorbing Nanoporous and Nanocomposite Thin Films. *J. Appl. Phys.* **2007**, *101*, No. 014320.
(79) Hutchinson, N. J.; Coquil, T.; Richman, E. K.; Tolbert, S. H.; Pilon, L. Reflectance of Surfactant-Templated Mesoporous Silica Thin Films: Simulations versus Experiments. *Thin Solid Films* **2010**, *518*, 2134−2140.
(80) Navid, A.; Pilon, L. Effect of Polarization and Morphology on the Optical Properties of Absorbing Nanoporous Thin Films. *Thin Solid Films* **2008**, *516*, 4159−4167.
(81) Jonasz, M.; Fournier, G. R. Refractive Indices and Morphologies of Aquatic Particles. In *Light Scattering by Particles in Water*, Elsevier, 2007; pp 447−558.

https://doi.org/10.1021/acsomega.1c06343
ACS Omega 2022, 7, 17519−17527